Engineering Fracture Mechanics 268 (2022) 108511

Contents lists available at ScienceDirect

Engineering Fracture Mechanics

journal homepage: www.elsevier.com/locate/engfracmech

Simulation of ductile-to-brittle transition combining complete Gurson model and CZM with application to hydrogen embrittlement

Meichao Lin [a], Haiyang Yu [b,**], Yu Ding [a], Vigdis Olden [c], Antonio Alvaro [c,d], Jianying He [a], Zhiliang Zhang [a,*]

[a] Department of Structural Engineering, Norwegian University of Science and Technology (NTNU), Trondheim 7491, Norway
[b] Division of Applied Mechanics, Department of Materials Science and Engineering, Uppsala University, Uppsala SE-75121, Sweden
[c] SINTEF Industry, Trondheim 7456, Norway
[d] Department of Mechanical and Industrial Engineering, Norwegian University of Science and Technology (NTNU), Trondheim 7491, Norway

ARTICLE INFO

Keywords:
Ductile-to-brittle transition
Complete Gurson model
Cohesive zone model
Hydrogen embrittlement

ABSTRACT

A general simulation framework for modelling ductile-to-brittle transition in metals is proposed. The method combines the complete Gurson model and cohesive zone model, which brings ductile and brittle fracture mechanisms into one play. We found that the transition of failure mode is the result of a competition between fracture due to micro-void growth and coalescence and fracture in the cohesive zone. It is found that the fracture mode is dependent on the ratio between the cohesive strength and the yield strength of the material; brittle fracture only occurs when the strength ratio is below a critical value. This generic rule can be used to rationalize various failure scenarios featured by ductile-to-brittle transition, such as low temperature embrittlement and hydrogen embrittlement. As an application of the general framework, hydrogen embrittlement is simulated. It is revealed that a critical hydrogen concentration has to be achieved in order to trigger brittle fracture, which is consistent with many experimental observations.

1. Introduction

Embrittlement is a type of environmentally-assisted fracture, which can occur under low temperature condition [1–4], upon irradiation [5] or due to the absorption of solute atoms such as hydrogen [6–10] and oxygen [11]. A common feature of embrittlement is a transition from ductile fracture with large plastic deformation to brittle fracture featured by limited plasticity, known as ductile-to-brittle transition (DBT), which brings these phenomena under a similar context. A numerical framework for modelling DBT in one certain condition is likely transferrable to or can provide inspiration for another and is of great importance for predicting embrittlement. In this work, two environmental factors, temperature and hydrogen, are considered.

Fracture of metallic material usually changes from ductile to brittle as the temperature decreases. The change is reflected in the energy absorption versus temperature curve which can be obtained from Charpy V-notched impact test, as illustrated in Fig. 1(a). The curve typically exhibits an 'S' shape with three regions recognized as the upper shelf, the transition phase and the lower shelf. Fracture

* Corresponding author.
** Corresponding author.
E-mail addresses: haiyang.yu@angstrom.uu.se (H. Yu), zhiliang.zhang@ntnu.no (Z. Zhang).

https://doi.org/10.1016/j.engfracmech.2022.108511
Received 19 October 2021; Received in revised form 27 April 2022; Accepted 28 April 2022
Available online 4 May 2022

Nomenclature

I_δ	Relative plasticity loss
C_H	Hydrogen concentration
C_i	Initial hydrogen concentration
C_{Hc}	Critical hydrogen concentration
σ_e	Conventional von Mises equivalent stress
$\overline{\sigma}$	Flow stress
f	Void volume fraction
σ_m	Mean stress
f_0	Initial void volume fraction
f_c	Critical void volume fraction
$\sigma_I^{Homogenous}$	Applied maximum principal stress
$\sigma_I^{Localized}$	Ability to resist localized deformation
σ_0	Yield strength
E	Young's modulus
$\overline{\varepsilon}$	Equivalent plastic strain
n	Hardening exponent
σ_c	Cohesive strength
δ_c	Critical separation
Γ_c	Cohesive energy
$\sigma_c(\theta)$	Cohesive stress with hydrogen
$\sigma_c(0)$	Cohesive stress without hydrogen
θ	Hydrogen coverage
R	Gas constant
Δg_b^0	Gibbs free energy-difference between the surface and the bulk
T	Temperature
σ_e	Engineering stress
ε	True strain
ε_f	Failure strain
γ	Strength ratio calculated as σ_c/σ_0
γ_c	The transition ratio
ε_{fG}	Ductile failure strain
PEEQ	Equivalent plastic strain
DBT	Ductile to brittle transition
DBTT	Ductile to brittle transition temperature
RRA	Relative reduction in area
HE	Hydrogen embrittlement
HEDE	Hydrogen enhanced decohesion
HELP	Hydrogen enhanced localized plasticity
CGM	Complete Gurson model
CZM	Cohesive zone model
TSL	Traction separation law
UEL	User defined element

in the upper shelf is ductile and is usually a result of the micro-void process, while the lower shelf is brittle with unstable crack growth. The transition phase is the mixture of both fracture modes. A DBT temperature (DBTT), which signifies the beginning of failure mode transition, can be determined from the 'S' shape curve. The DBTT is chemical composition [1], grain size [2] and dislocation density [3] dependent. A material displaying higher DBTT (e.g. material B in Fig. 1a) is more prone to unstable brittle fracture than the material with lower DBTT (e.g. material A in Fig. 1a). Suppressed dislocation activity [12] and reduced interfacial strength [13,14] are among the principal causes for the DBT phenomena at low temperature.

Many metallic materials also suffer from a serious loss of ductility and decrease in resistance to cracking when exposed to hydrogen environment, in a phenomenon referred to as hydrogen embrittlement (HE) [6–10,15]. The loss in ductility can be scaled by relative plasticity loss (I_δ) [16], relative reduction in area (RRA) [17] and relative reduction in tension strength and impact strength [18], which can be directly measured in experiments. Djukic et al [18] made a summary that there existed an inverted 'S' shape curve to describe various mechanical characteristics, i.e. ductility, yield strength, ultimate tension strength and impact strength, versus hydrogen concentration C_H, which is comparable to the curve in Fig. 1a. Therefore, there seems to be a strong phenomenological resemblance between low temperature embrittlement and HE. Analogously as the DBTT, there exists a critical hydrogen content C_{Hc}

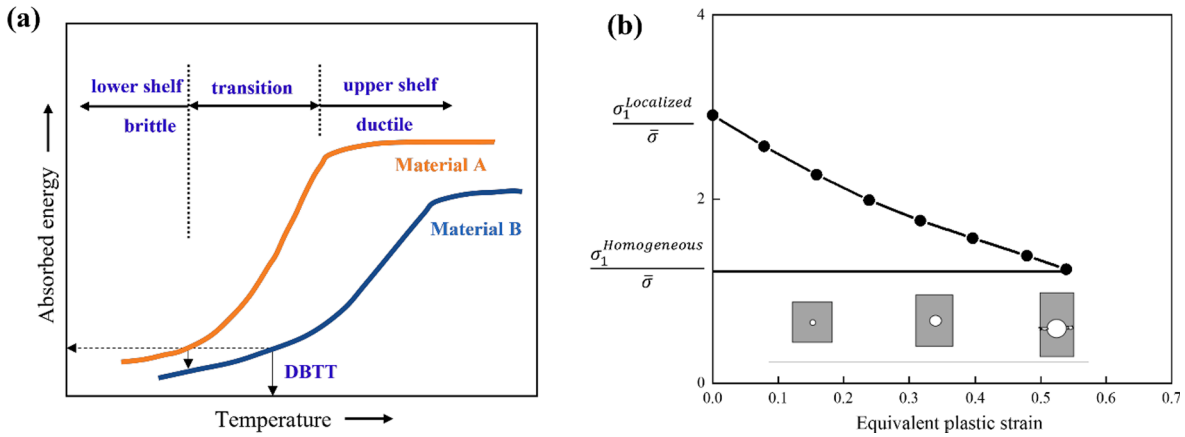

Fig. 1. (a) Schematic of absorbed energy (fracture toughness) versus temperature curve of two materials; (b) Illustration of the competition between the homogenous and localized deformation modes in the CGM, the plot is reproduced based on the data from [37].

over which brittle fracture is triggered, and the value of C_{Hc} is dependent on alloy composition, microstructure, experimental condition and stress/strain level [7,19–21]. Typically, the hydrogen-induced ductility loss is related to the change of fracture mode: the fractography changes macroscopically from a cup-and-cone to a flat configuration, and from dimpled to intergranular or cleavage facets microscopically when exposed to hydrogen environment; stronger the loss of ductility and proportionally more pronounced are the cleavage and quasi-cleavage facets over the dimpled areas on the fracture surface [22,23]. Many theories have been proposed to rationalize the various HE phenomena, among which the hydrogen enhanced decohesion (HEDE) mechanism and the hydrogen enhanced localized plasticity (HELP) mechanism are widely adopted. The HEDE mechanism assumes that hydrogen weakens the cohesive strength of the interatomic bonds in the lattice [24], leading to brittle fracture. The HELP mechanism states that hydrogen facilitates dislocation motion which enhances localized plasticity [25].

As presented above, the ductility of metals is generally reduced as temperature is decreased or hydrogen concentration is increased, as a result of decreased portion of ductile fracture and increased portion of brittle fracture. The fracture toughness reaches the lower shelf (Fig. 1a) when brittle fracture becomes the sole type. Independently from the cause, phenomenologically a DBT can be rationalized as the competition between ductile and brittle fracture, which can be simulated by combining both fracture types in a numerical framework.

It is well established that ductile fracture in metals is the result of the process including the nucleation, growth and coalescence of micro-voids. Substantial effort has been devoted into developing void based micromechanical models [26–28], and among these, the one introduced by Gurson [29], later modified by Tvergaard and Needleman [30] (GTN model) is probably the most recognized in the scientific community. The GTN model is endowed with a yield function, a flow law, a rule for nucleating voids, a criterion for evolution of the voids, and takes void volume fraction as damage variable, with which the softening effects, as well as ductile fracture process of the material are well modelled. Brittle fracture, on the other hand, entails a sudden and unstable crack growth immediately after a crack is nucleated. Among the different models [31–33] which can be utilized to represent a brittle failure, the cohesive zone model (CZM) is attractive thanks to its simplicity and its physical relevance as detailed in [34]. Some attempts to utilize the aforementioned models in the same framework were made by Hütter et al [35] who combined the GTN model with CZM to simulate crack propagation in a boundary layer model. Machado et al [36] also associated GTN model with CZM and studied the R-curve of a crack containing model in uniaxial tension specimen. Zhang [37] proposed a so-called complete Gurson model (CGM) by incorporating the GTN model with the plastic limit model [38], which enables the detection of void coalescence without artificially introducing a void coalescence criterion.

In this work, the CGM is adopted to represent ductile fracture while a CZM approach based on a polynomial traction separation law (TSL) [39] is used to model the brittle fracture. A parametric study has been conducted to feature and investigate the DBT behavior. Further, a three-step hydrogen informed CZM approach [40–42] is employed to simulate the influence of hydrogen on DBT. The paper is organized as follows. In Section 2, the CGM and CZM methods are introduced. Section 3 presents the results and discussion, highlighting the influence of different material parameters on the DBT. In Section 4, hydrogen induced DBT is simulated as a case study, and the physical meaning behind the transition is illustrated. The main conclusions are summarized in Section 5.

2. Methodology

2.1. Complete Gurson model

The Gurson model analyzes the plastic flow in a porous medium assuming that the material behaves as a continuum. Voids appear in the model indirectly through their influence on the global flow behavior [43]. The yield function of the Gurson model is derived by 'smearing' the micro-voids across the material and performing the rigid-plastic upper bound analysis [44].

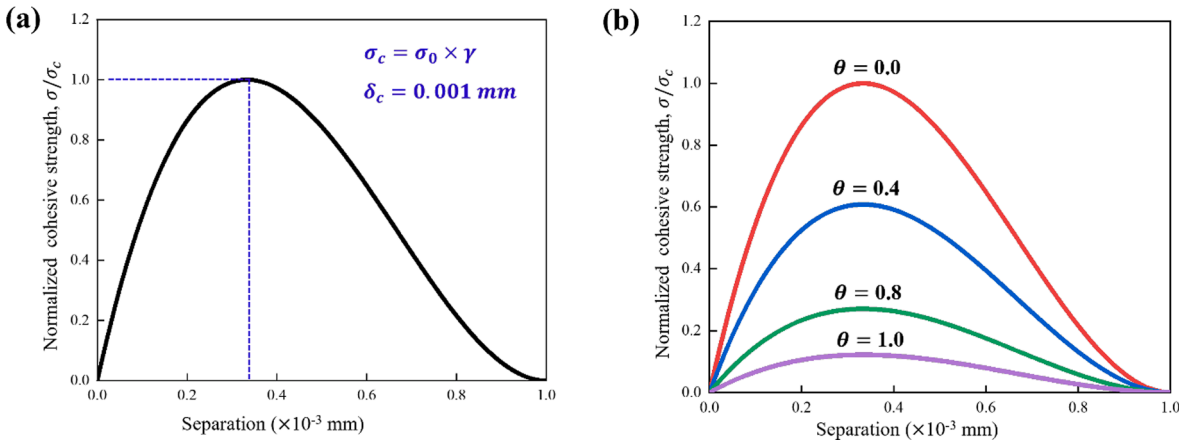

Fig. 2. (a) Illustration of a polynomial TSL; (b) Hydrogen degraded TSL curves with different hydrogen coverage θ.

$$(\frac{\sigma_e}{\overline{\sigma}})^2 + 2q_1 f cosh\left(\frac{3q_2\sigma_m}{2\overline{\sigma}}\right) - 1 - q_3 f^2 = 0 \tag{1}$$

σ_e is the conventional von Mises equivalent stress, $\overline{\sigma}$ is the flow stress of the matrix material, f is the void volume fraction and σ_m is the mean stress. q_1, q_2 and $q_3 = q_1^2$ are the fitting parameters introduced to enhance the accuracy of prediction [30]. The original Gurson model is retrieved by setting $q_1 = q_2 = 1$.

Failure inherent to the micro-void process can be divided into two stages, homogenous deformation with void nucleation and growth, and localized deformation leading to void coalescence. The GTN model can well represent the homogenous deformation phase, i.e. void growth. To predict void coalescence, a critical void volume fraction criterion is often used. The criterion assumes that void coalescence occurs when a critical void volume fraction f_c is reached [30]. Usually, f_c is empirically selected or numerically fitted from experiments [30,45], which may result in non-unique problem [46]. To address this issue and attach a physically based coalescence criterion to Gurson model, CGM is proposed [37]. The Thomason's plastic limit load model [38] is incorporated into the CGM, which considers the competition between the homogenous deformation mode and localized deformation mode, as illustrated in Fig. 1 (b). The void coalescence happens when:

$$\sigma_I^{Homogenous} = \sigma_I^{Localized} \tag{2}$$

$\sigma_I^{Homogenous}$ represents the applied maximum principal stress at the current yield surface, $\sigma_I^{Localized}$ represents the micro-capacity of a voided material to resist localized deformation. In this way, f_c can be automatically determined. The ductile fracture process is hence only linked to the void nucleation parameters and the flow properties of the matrix material. In the present work, void nucleation is represented by the cluster nucleation model [37], which is applicable to many engineering materials. For the nucleation model [37], it is usually assumed that voids will be nucleated in the beginning of plastic deformation and the only controlling parameter is the initial void volume fraction f_0. Apparently, $f_0 = 0$ represents the scenario without initial void, and Eq. (1) reduces to:

$$(\frac{\sigma_e}{\overline{\sigma}})^2 - 1 = 0 \tag{3}$$

which retrieves the von Mises yield surface. A parametric power law is used to describe the hardening property of the matrix material [35].

$$\frac{\overline{\sigma}}{\sigma_0} = \left(\frac{\overline{\sigma}}{\sigma_0} + \frac{E}{\sigma_0}\overline{\varepsilon}\right)^n \tag{4}$$

$\overline{\varepsilon}$ is the equivalent plastic strain, σ_0 is the yield stress, n is the hardening exponent, E is Young's modulus. The CGM is implemented in ABAQUS through a UMAT subroutine[1] with efficient numerical algorithms developed by Zhang [47].

2.2. Cohesive zone model

The brittle fracture is simulated by CZM. The constitutive behavior of cohesive elements is controlled by a polynomial TSL [39].

[1] A free copy of the UMAT source code can be obtained from the corresponding author.

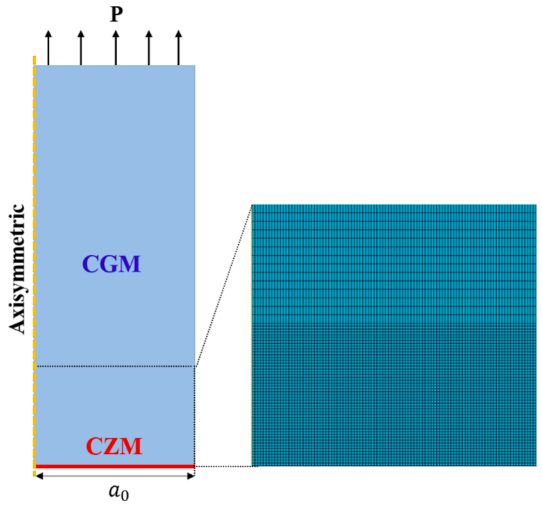

Fig. 3. Sketch of the smooth tensile bar model and a zoom-in view of the mesh near the cohesive zone area. Only a quarter of the specimen is modelled due to axi-symmetry.

$$\sigma(\delta) = \begin{cases} \frac{27}{4}\sigma_c \frac{\delta}{\delta_c}\left(1 - \frac{\delta}{\delta_c}\right)^2 & \delta \le \delta_c \\ 0 & \delta > \delta_c \end{cases} \tag{5}$$

σ_c is the cohesive strength, δ_c is the critical separation, $\sigma(\delta)$ and δ are stress and separation of the cohesive element. An illustration of this TSL is found in Fig. 2(a). Upon loading, the cohesive stress inside the cohesive element first increases until σ_c is reached, material degradation (softening) then follows, and complete failure occurs when the critical separation δ_c is reached. The area below the traction separation curve is defined as cohesive energy Γ_c, a measurement of fracture toughness. In finite element modelling, it is possible to take advantage of the symmetry of a problem. There are two approaches of applying symmetric boundary conditions to the cohesive elements, as detailed in [48,49]. In this work, linear constraint equations are applied to the corresponding nodes on the upper and lower cohesive surfaces, according to [48,49]. The CZM simulation is realized with a user defined element (UEL) subroutine, introduced in [50] and revised by the current authors.

When it comes to the simulation of hydrogen induced fracture, the hydrogen informed CZM approach [40,51] is used, which is realized in three steps, as detailed in [52,53]. The σ_c is assumed to decrease with increasing hydrogen content, consistent with the HEDE mechanism and is described by a hydrogen degradation law suggested for H/Fe system [54,55]. This degradation law has been applied to pipeline steel [56], low alloy steel [57], duplex stainless steel [58–60] etc., and is used as a general example in our case study.

$$\frac{\sigma_c(\theta)}{\sigma_c(0)} = 1 - 1.0467\theta + 0.1687\theta^2 \tag{6}$$

$$\theta = \frac{C_H}{C_H + exp(-\Delta g_b^0/RT)} \tag{7}$$

$\sigma_c(0)$ is the cohesive stress without hydrogen, θ is hydrogen coverage, $\sigma_c(\theta)$ is the cohesive stress with hydrogen, C_H is the hydrogen concentration, Δg_b^0 is the Gibbs free energy-difference between the surface and the bulk, R is the gas constant, T is the temperature.

2.3. Numerical procedure

The specimen simulated in this work is a smooth tensile bar, with a length of 200 μm and a radius of 40 μm. Due to its axi-symmetry, only a quarter of the specimen is modelled. The sketch of the model is shown in Fig. 3. Loading is displacement controlled. Axisymmetric CAX4 elements are used in the bulk which is defined as CGM material. Brittle fracture is assumed to occur in the middle of the specimen and perpendicular to the loading direction, a layer of cohesive elements is inserted along the bottom line of the quarter model (Fig. 3). This is acceptable for the case of hydrogen induced fracture in round tensile bars, as evidenced in the experiment [61]. However, it should be noted that for a flat specimen, the fracture path may not be perpendicular to the loading direction, then inclined

Table 1
The constant parameters used in the simulation [66–69].

Parameters used in the stress analysis					
E(GPa)	υ	δ_c(mm)	q_1	q_2	q_3
200	0.3	0.001	1.5	1.0	2.25
Parameters used in the hydrogen diffusion analysis					
Diffusivity (m^2/s)		Solubility ($ppm\,mm\,N^{-1/2}$)	Δg_b^0(kJ/mol)	R (J/K/mol)	T (K)
6×10^{-11} [66,67]		0.033 [66,67]	30 [69]	8.314	298

cohesive layers should be inserted to model that scenario. The symmetric boundary condition is realized by applying linear constraint equations to the cohesive nodes. The minimum mesh size near the cohesive zone is 0.4 μm × 0.4 μm, relatively coarse mesh is applied in the remaining part. The minimum mesh size is selected based on a convergence study. A zoom-in view of the mesh close to the cohesive zone is shown in Fig. 3. With this model, ductile fracture with void coalescence and brittle fracture in the cohesive elements can be captured by CGM and CZM, respectively.

With the applied CGM model, a set of three parameters (f_0, σ_0, n) can be used to characterize the plastic deformation and ductile fracture behavior for a given material. A series of numerical analyses with f_0 varying from 0 to 0.1 [62,63], σ_0 varying from 400 MPa to 1000 MPa [64,65], and n varying from 0.05 to 0.2 [64,65] are performed. For each combination of (f_0, σ_0, n), different values of cohesive strength σ_c are selected to investigate the DBT behavior. The other parameters are kept constant, as listed in Table 1. Hereinafter, the term 'material' means a combination of parameters (f_0, σ_0, n) that represent a certain material behavior, as this is a parametric study.

2.4. Definition of failure strain

During a tensile test, the engineering stress σ_e is calculated dividing the load P by the initial cross-sectional area.

$$\sigma_e = P/\pi a_0^2 \tag{8}$$

The true strain ε is calculated as:

$$\varepsilon = 2 \times \ln(a_0/a) \tag{9}$$

a_0 and a are the initial minimum cross-sectional radius and the instantaneous minimum cross-sectional radius under loading, respectively. The engineering stress-true strain curve (σ_e-ε) is plotted, since the true strain is usually independent of initial specimen length [70]. The failure strain ε_f refers to the true strain corresponding to the apparent sudden drop of the engineering stress σ_e.

3. Results and discussion

3.1. Ductile fracture and brittle fracture

For a given 'material', i.e., a certain combination of (f_0, σ_0, n), both ductile fracture and brittle fracture can be captured by applying different cohesive strength σ_c. For instance, with ($f_0 = 0.001$, $\sigma_0 = 400$ MPa, $n = 0.1$) and $\sigma_c = 720$ MPa, ductile fracture happens with failure occurring in the bulk region (CGM material), as shown in Fig. 4(a); with ($f_0 = 0.001$, $\sigma_0 = 400$ MPa, $n = 0.1$) and $\sigma_c = 480$ MPa , however, brittle fracture along the central cohesive zone occurs, as shown in Fig. 4 (b). In the former case, significant plasticity with evident necking occurred which indicates substantial void growth and inter-void coalescence. On the other hand, limited plasticity is observed in the latter case: crack propagates along the cohesive zone, indicating a brittle fracture. Therefore, the proposed numerical approach can capture both ductile and brittle fracture, and it offers the potential of investigating the competition/transition between these two fracture modes upon parametric study.

Comparing the two cases in Fig. 4, one can tell that the only difference is σ_c, which characterizes the strength of the cohesive layer. If substantial plasticity can be triggered before this assigned cohesive strength is reached, failure will be mostly ductile, otherwise, brittle crack initiation and propagation may occur, releasing stress and suppressing plasticity. Considering that one important parameter for plasticity is the yield strength σ_0 and the initiation of brittle fracture is strength (σ_c) controlled, a strength ratio $\gamma = \sigma_c/\sigma_0$ is introduced as the major variable to give a quantified description of the transition between the two failure modes. In subsequent parametric studies, two general scenarios are considered: with ($f_0 > 0$) and without initial void ($f_0 = 0$).

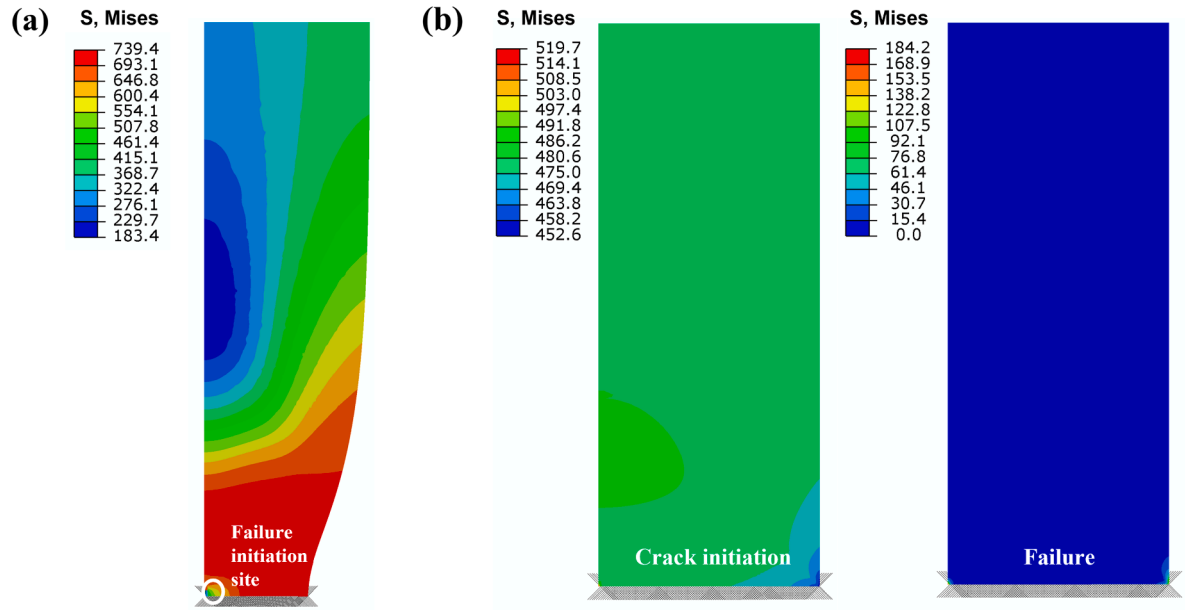

Fig.4. Illustration of (a) ductile fracture and (b) brittle fracture, the crack initiation defines as the failure of the first element. The same parameters of ($f_0 = 0.001$, $\sigma_0 = 400$ MPa, $n = 0.1$) are assigned, the cohesive strength $\sigma_c = 720$ MPa for (a) and $\sigma_c = 480$ MPa for (b).

3.2. *Transition of fracture mode: the scenario without initial void*

For the scenario without initial voids, i.e. ($f_0 = 0$, σ_0, n), von Mises material behavior is retrieved, failure cannot occur by void coalescence since the ductile failure criterion is not defined, but the loss in loading bearing capacity can still be observed due to plastic instability (necking). Obviously in such scenario, the specimen can fail uniquely by the damage represented through the cohesive layer. This simple scenario enables us to study the competition between the two failure modes without the interference of void induced ductile fracture.

The engineering stress-true strain (σ_e- ε) curves with$f_0 = 0$, σ_0= 400 MPa, $n = 0.1$ and $\gamma = 1.4$, 1.5, 1.6, 1.7, 1.8, 2.0 are presented in Fig. 5. The engineering stress σ_e descreases after reaching the maximum value, displaying a global softening effect induced by necking; the true strain corresponding to the maximum value of engineering stress is approximately equal to the hardening exponent, seen in the pink line in Fig. 5, which is consistent with the empirical relation in [71,72]. The failure strain ε_f increases with γ, since a larger cohesive strength σ_c (larger γ) means a stronger cohesive layer, which naturally results in a larger global failure strain ε_f. When γ is small, e.g. $\gamma = 1.4$ in this figure, failure happens quite early, even before the peak stress is reached, indicating that global softening has

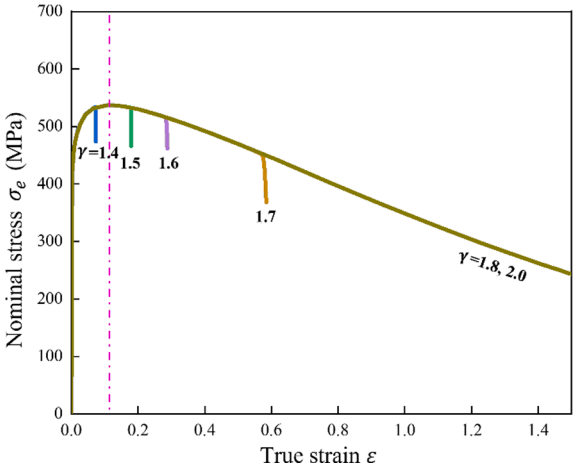

Fig. 5. The engineering stress σ_e versus true strain ε curves with $f_0 = 0$, $\sigma_0 = 400$ MPa, $n = 0.1$ and different γ. Failure occurs in the cohesive layer up to $\gamma = 1.7$, while failure is completely controlled by necking when $\gamma > 1.7$. The pink line indicates that the true strain corresponding to the maximum value of engineering stress is approximately equal to the hardening exponent. (For interpretation of the references to colour in this figure legend, the reader is referred to the web version of this article.)

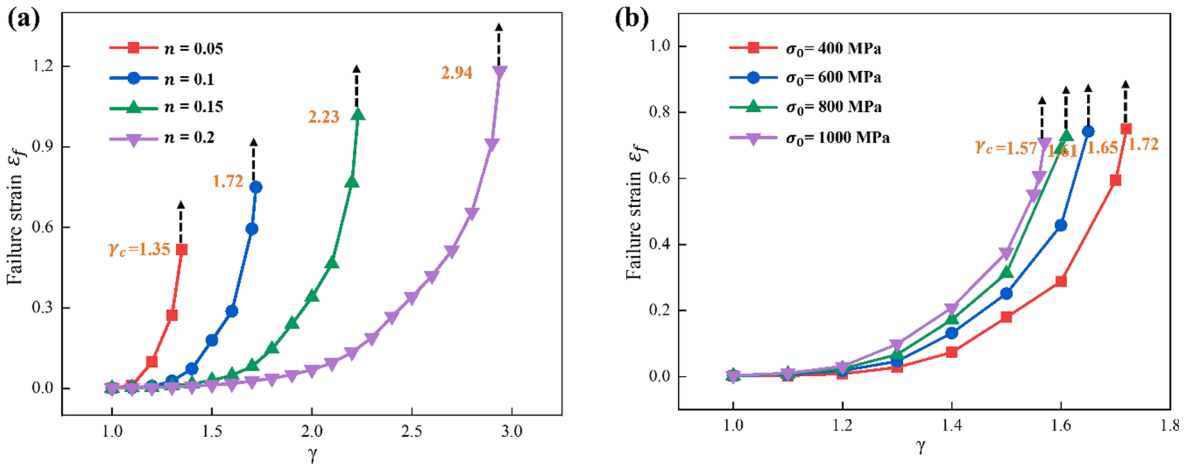

Fig. 6. (a) The failure strain ε_f versus γ with$f_0 = 0$, σ_0= 400 MPa and varying n; (b) ε_f versus γ with$f_0 = 0$, $n = 0.1$ and varying σ_0. In both cases, there exist a transition ratio γ_c beyond which failure no longer occurs in the cohesive layer, the ε_f becomes 'infinite' due to the lack of a damage criterion in the matrix (von Mises) material behavior.

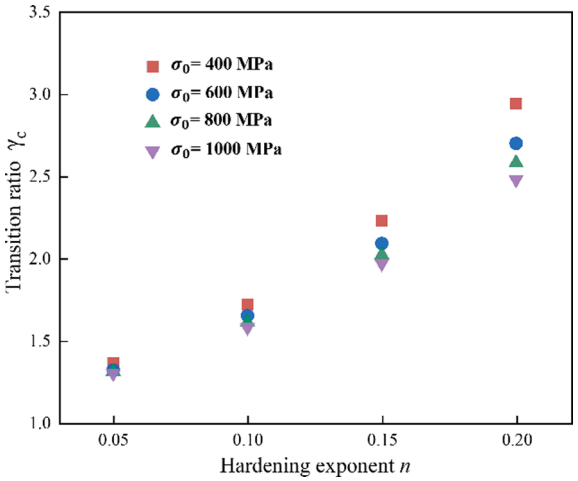

Fig. 7. The transition ratio γ_c versus n, σ_0 with $f_0 = 0$. The transition ratio γ_c increases with n while decreases with σ_0.

not started or substantial plasticity has not been triggered, so failure in this case is mainly of brittle type, comparable to that in Fig. 4 (b). As γ increases, global softening becomes more significant; meanwhile, due to the loss in global load bearing capacity, the cohesive layer becomes less prone to failure. Considering that cohesive fracture is the only possible failure mode (i.e. actual separation of material) in this scenario, we expect there to be a unique case with a particular ratio γ above which no failure will occur. Apparently, the special case is $\gamma = 1.7$ in Fig. 5. ε_f tends to an 'infinite' value for $\gamma > 1.7$, meaning that the specimen fails completely due to necking. It indicates a complete transition of the fracture mode: fracture is no longer controlled by CZM, but fully controlled by the plasticity of von Mises material. The value of γ in the transition case is an important parameter for DBT, which is then defined as the transition ratio γ_c. Similar transition cases are also observed in other series of simulations, which have different plasticity properties. It should be noted that the critical separation δ_c of the cohesive element has limited influence on this transition ratio γ_c, as demonstrated in Appendix A, since brittle fracture initiation is stress controlled and δ_c has minor influence on the local stress, as long as it is not exceedingly large.

'Material' with different plasticity properties represented by ($f_0 = 0$, σ_0, n) are further simulated, where n and σ_0 are set as $n =$ 0.05, 0.1, 0.15, 0.2 and $\sigma_0 =$ 400 MPa, 600 MPa, 800 MPa, 1000 MPa, respectively, following orthogonal design principle [73]. The failure strain ε_f versus γ curves with $f_0 = 0$, $\sigma_0 = 400$ MPa and varying n are presented in Fig. 6(a). As expected, ε_f increases with the increase of γ in each curve; ε_f approaches infinity after a critical strength ratio in all the cases, these are consistent with the results in Fig. 5 where a transition ratio γ_c exists and no failure is detected in the cohesive layer beyond this ratio. The transition ratio γ_c increases from 1.35 to 2.94 with n ranging from 0.05 to 0.2, since higher stress is built up in the matrix with bigger hardening exponent n, as in Eq. (4). The ε_f versus γ curves with $f_0 = 0$, $n = 0.1$ and varying σ_0 are shown in Fig. 6(b). Similarly, a transition of fracture mode exists for each σ_0, however the transition ratio γ_c decreases from 1.72 to 1.57 when σ_0 increases from 400 MPa to 1000 MPa. This is because

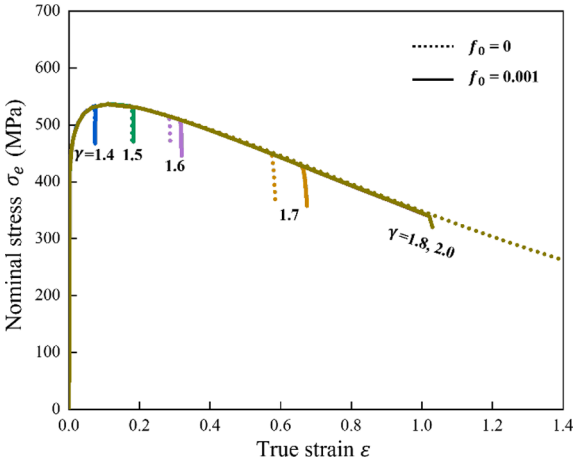

Fig. 8. The comparison of engineering stress σ_e versus true strain ε curves with and without initial voids at different γ. The failure strain ε_f in the$f_0 = 0.001$ case is always larger than that in the$f_0 = 0$ case when $\gamma < \gamma_c$; the ε_f is no longer infinite when $\gamma > \gamma_c$ for$f_0 = 0.001$ case.

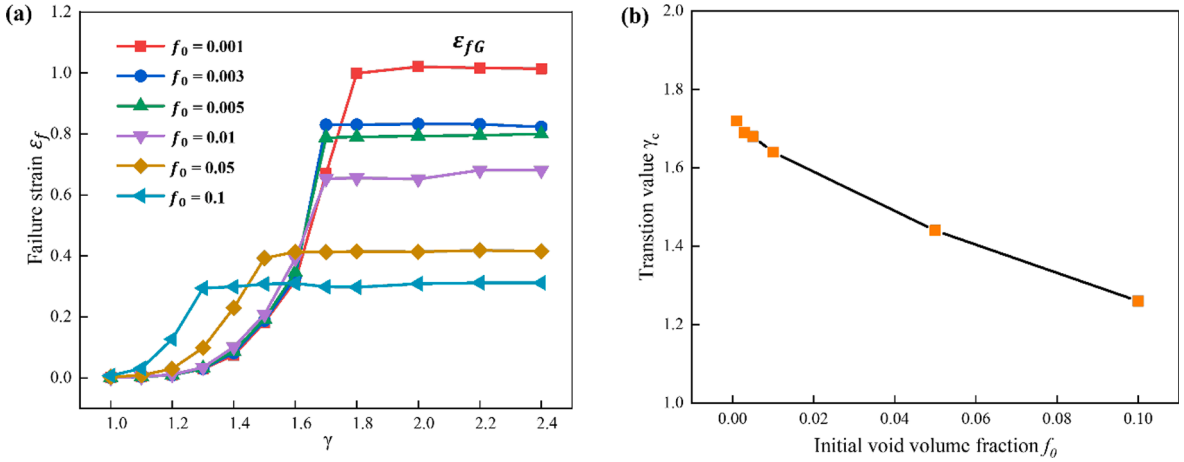

Fig. 9. (a) Failure strain ε_f versus γ with$\sigma_0 = 400$ MPa, $n = 0.1$ and varying f_0; (b) The transition ratio γ_c versus f_0 with$\sigma_0 = 400$ MPa, $n = 0.1$. In the brittle regime, ε_f increases with f_0 for a certain γ; in the ductile regime, ductile failure strain ε_{fG} decreases with f_0; γ_c decreases with f_0.

lower stress is built up in the matrix with bigger σ_0, considering that the same Young's modulus is adopted, as also revealed in Eq. (4). The transition ratio γ_c is further plotted against n and σ_0 in Fig. 7. To sum up, γ_c increases with the hardening exponent n while it decreases with the yield strength σ_0; the influence of n on γ_c is more pronounced.

As elaborated earlier, failure can never happen in the cohesive zone when $\gamma > \gamma_c$, rather, it happens in the bulk which can fail only by necking. In other words, there exists a threshold cohesive strength beyond which the cohesive layer never fails, for a given 'material' ($f_0 = 0$, σ_0, n). Through verification, it is found that the threshold cohesive strength also exists when applying a linear TSL. We further verified that if the bulk material is assumed linear elastic, i.e., $\sigma_0 \to \infty$, then such a threshold value does not exist (which is expected as $\gamma \to 0$ for linear elastic materials). Therefore, the existence of the transition value γ_c should be interpreted as the interaction between the cohesive zone and plasticity. The key feature of cohesive zone fracture is the existence of a fracture process zone across which the critical opening stress has to be reached [74], this is different from the conventional stress-based failure criterion where the critical stress only needs to be achieved at a point. In the case with plasticity and for high values of cohesive strength, plasticity-induced localization (necking) can occur, which leads to stress concentration at the center of the specimen. The cohesive strength can be achieved at the center followed by cohesive degradation as shown in Fig. 2; this leads to local softening which releases the opening stress in the elements nearby. When the cohesive strength is higher than a threshold value, the fracture criterion is no longer fulfilled across the fracture process zone, therefore the cohesive elements will not fail. Similar situation is observed in CZM modelling of specimens with a pre-existing crack or notch [35]. Finally, in the case of linear elasticity, the opening stress distributes uniformly over the cross-section of the smooth bar and local softening does not occur, so there is not a threshold cohesive strength when plasticity is not considered. The same principle also applies to the scenario with initial voids, where local softening is contributed not only by the cohesive elements, but also by the matrix due to the growth of voids.

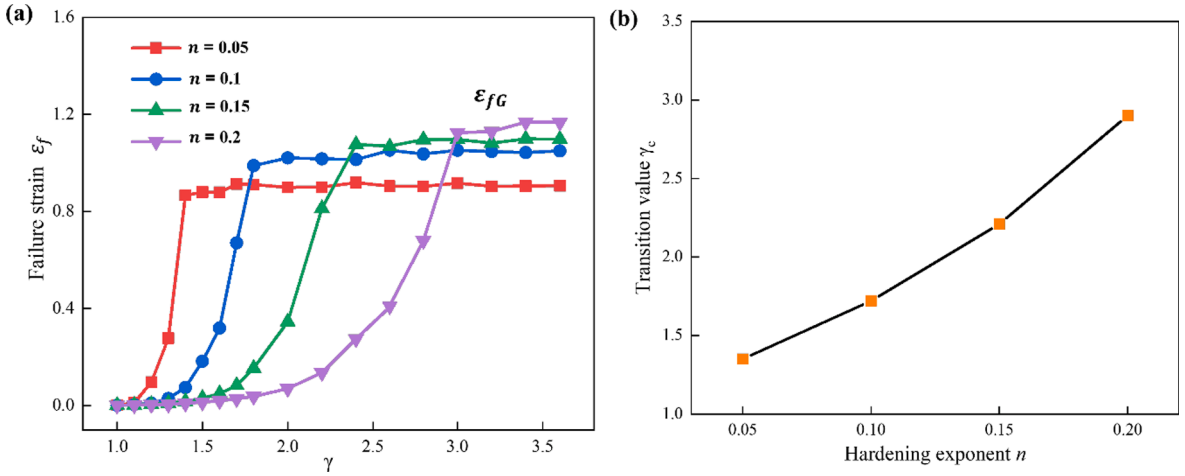

Fig. 10. (a) Failure strain ε_f versus γ with $f_0 = 0.001$, $\sigma_0 = 400$ MPa and varying hardening exponent n; (b) The transition ratio γ_c versus n with $f_0 = 0.001$, $\sigma_0 = 400$ MPa. Ductile failure strain ε_{fG} increases with n; γ_c increases with n.

3.3. *Ductile-brittle transition: the scenario with initial void volume fraction*

For the 'material' with the presence of initial voids ($f_0 > 0$), the yield criterion follows Eq. (1) and the failure criterion by void coalescence follows Eq. (2). The engineering stress-true strain (σ_e- ε) curves with and without intial voids are shown in Fig. 8 for comparison. When the ratio γ is small, the failure strain ε_f increases with γ, similar to that without initial void ($f_0 = 0$) as shown in Fig. 5; there also exists a transition ratio γ_c above which failure no longer happens in the cohesive zone. Unlike the scenario with$f_0 = 0$, ε_f does not become infinite for $\gamma > \gamma_c$, but rather approaches a constant value, which is defined as the ductile failure strain ε_{fG}, the suffix 'G' reflects the fact that failure happens in Gurson material. Interestingly, under the condition $\gamma < \gamma_c$ (CZM controlled fracture), ε_f in the$f_0 = 0.001$ case is always larger than that in the $f_0 = 0$ case, indicating that the matrix with initial voids is more resistant to brittle failure than that without initial void, which is seemingly counter-intuitive. The reason is that failure happens in the cohesive zone instead of in the porous bulk, the case with initial voids has softer mechanical response and consequently reduced level of opening stress in the cohesive zone, which delays the failure of cohesive elements and globally gives a higher ε_f. The same principle applies to the cases with different levels of initial void volume fraction. For a given γ, the 'material' with a larger initial void volume fraction (larger f_0) displays a higher ε_f value than those 'material' with a lower f_0 value in the case failure occurs in the cohesive zone ($\gamma < \gamma_c$), as shown in Fig. 9(a).

The failure strain ε_f versus γ curves with $\sigma_0 = 400$ MPa, $n = 0.1$ and varying f_0 are shown in Fig. 9(a). ε_f increases at first with growing γ and reaches a constant value ε_{fG}, indicating a transition from brittle (CZM) to ductile (CGM) fracture. In the brittle regime, for a certain γ, ε_f increases with f_0 as mentioned earlier, and in the ductile regime ε_{fG} decreases with the increase of f_0, which is expected in a conventional porous material. The transition ratio γ_c versus f_0 relation is plotted in Fig. 9(b). γ_c decreases with f_0. It has been shown earlier that the dominant fracture mode shifts from ductile to brittle as γ decreases below γ_c. The results so far indicate a limited influence of f_0 in practice, since f_0 is usually much smaller than 0.01 in a real material.

A key difference between the scenarios with and without initial void is that the ε_f versus γ curve in Fig. 9(a) exhibits an 'S' shape with an upper plateau due to the existence of a finite ε_f in the ductile regime. In all the curves a 'sharp' transition to the upper plateau is observed, this is because a homogenous specimen is simulated and the CZM and CGM fracture are mutually exclusive in the current model. If microstructural features in the specimen are considered and a mixture of CZM and CGM failure allowed, a smooth transition, and hence a smooth 'S' curve, is expected. In addition, preliminary studies (not added here for the sake of brevity) have shown that the 'S' shape also holds for notched tensile specimens. The ductile failure strain ε_{fG} is independent of γ, since it is completely controlled by Eqs. (1) and (2). Phenomenologically, the curves are comparable to the low temperature DBT curve in Fig. 1(a). The ordinates, absorbed energy and failure strain, are both measurements of the material's resistance to fracture; the abscissa, $\gamma = \sigma_c/\sigma_0$ in Fig. 9(a), essentially scales the model's tendency to undergo brittle fracture. This tendency is influenced by environmental factors, such as temperature which is the abscissa in Fig. 1(a); with the increase of temperature, a larger portion of ductile fracture tends to occur, equivalent to having a rising γ. The curve in Fig. 1(a) displays a brittle fracture plateau on the low temperature side and a ductile plateau on the high temperature side, the same as Fig. 9(a). Another environmental factor is hydrogen, as also mentioned in the Introduction. The only difference from a phenomenological point of view is that fracture tends to transit from the ductile regime to the brittle regime with the increase of hydrogen concentration, hence the ductile plateau is expected on the low hydrogen concentration side and the brittle plateau on the high hydrogen concentration side. In other words, an inverted 'S'-shaped curve is expected, such a curve is experimentally observed in [17] where the reduction in cross sectional area is plotted versus hydrogen concentration. In Section 4, an inverted 'S'-shaped curve is obtained by simulation.

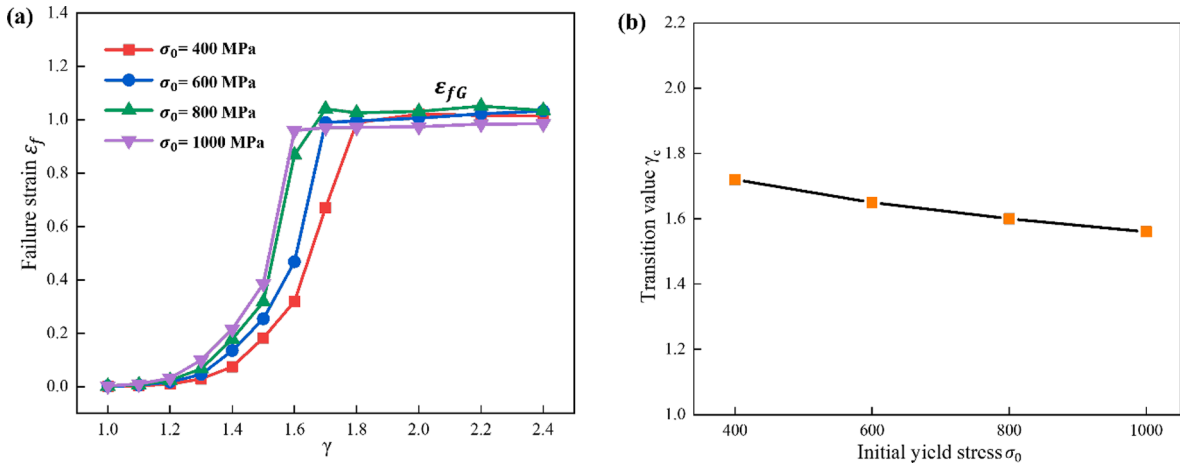

Fig. 11. (a) Failure strain ε_f versus γ with $f_0 = 0.001$, n= 0.1 and varying initial yield σ_0; (b) The transition ratio γ_c versus σ_0 with $f_0 = 0.001$, n = 0.1. σ_0 has minor effect on ductile failure strain ε_{fG}; γ_c decrease with σ_0.

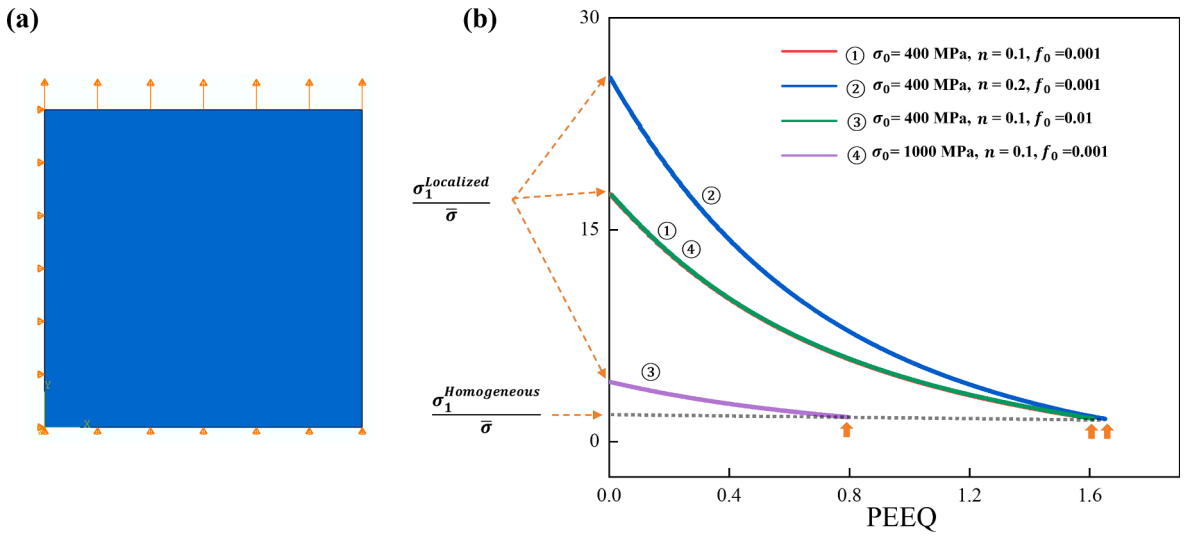

Fig. 12. (a) Sketch of the one element model used for the CGM simulation; (b) $\sigma_1^{Localized}/\bar{\sigma}$ and $\sigma_1^{Homogenous}/\bar{\sigma}$ versus PEEQ curves with different parameters. The arrows mark the PEEQ values of the intersecting points.

3.4. The influence of plasticity parameters on the transition

The initiation of DBT is an important material property: there is a DBTT in the case of low temperature embrittlement, and a critical hydrogen concentration C_{Hc} for HE [7,19–21]. In a general sense, both can be correlated to the transition ratio γ_c, with the failure strain ε_f being a function of temperature or hydrogen concentration.

The effect of the plasticity parameters (σ_0, n) on the ε_f and γ_c are then studied. The ε_f versus γ curves with $f_0 = 0.001$, $\sigma_0 = 400$ MPa and varing n are shown in Fig. 10(a), and the ε_f versus γ curves with $f_0 = 0.001$, $n = 0.1$ and varing σ_0 are shown in Fig. 11(a). Similarly, ε_f increases with increasing γ until the ductile failure strain ε_{fG} is reached. When $\gamma < \gamma_c$, what's happening in Fig. 10(a) is comparable to that in Fig. 6 (a), and what's happening in Fig. 11(a) is comparable to that in Fig. 6 (b). When $\gamma > \gamma_c$, ε_{fG} becomes independent of γ and relies on plasticity parameters. ε_{fG} increases with n, but shows minor dependence on σ_0. The γ_c versus n curve is plotted in Fig. 10(b), and the γ_c versus σ_0 curve is plotted in Fig. 11(b). γ_c increases with the hardening exponent n and decreases with growing yield strength σ_0, the same as the scenario without initial void.

In the following, the influence of the plasticity parameters (f_0, σ_0, n) on ε_{fG} is discussed by means of a single element model, as

shown in Fig. 12(a). The constitutive behavior of this element is described by CGM, following Eq.(1) and Eq.(2), and axi-symmetrical tension is applied. Recall Eq. (2), there are two competing deformation modes during loading, the homogenous deformation mode and the localized deformation mode. Which mode prevails is dependent on the magnitudes of $\sigma_1^{Localized}$ and $\sigma_1^{Homogenous}$. The $\sigma_1^{Localized}/\overline{\sigma}$ and $\sigma_1^{Homogenous}/\overline{\sigma}$ versus PEEQ curves with different material properties (f_0, σ_0, n) are plotted in Fig. 12(b). In the early stage of loading, $\sigma_1^{Homogenous}$ is smaller than $\sigma_1^{Localized}$, indicating that the homogenous deformation mode is the dominant path. As the plastic strain increases, $\sigma_1^{Localized}$ decreases until it equals $\sigma_1^{Homogenous}$, which represents the condition for inter-void necking (coalescence). Apparently, the dependence of ductile failure strain ε_{fG} roots in the dependence of $\sigma_1^{Localized}$ on the plasticity parameters. Comparing curve ① with ③, $\sigma_1^{Localized}/\overline{\sigma}$ is much smaller with a larger f_0, and the intersection with $\sigma_1^{Homogenous}/\overline{\sigma}$ occurs earlier, as marked with the arrow in Fig. 12 (b), therefore ε_{fG} decreases with f_0. Comparing curves ① with ④, $\sigma_1^{Localized}/\overline{\sigma}$ are practically the same with different σ_0, hence σ_0 has negligible influence on ε_{fG}. Comparing curve ① with ②, $\sigma_1^{Localized}/\overline{\sigma}$ is larger with a larger n, and the intersection with $\sigma_1^{Homogenous}/\overline{\sigma}$ occurs at larger PEEQ, a greater ε_{fG} is hence expected for a higher n.

4. Application to hydrogen embrittlement: A case study

So far, DBT has been simulated in a general sense. This phenomenon is rationalized as the competition between the tendency to fracture in a brittle way, simulated with CZM, and the tendency to fracture in a ductile manner, simulated with CGM. This can be correlated to low temperature embrittlement as well as HE.

In the case study here, two 'material' models, designated as M1 with (f_0, σ_0, n) = (0.001, 400 MPa, 0.1) and M2 with (f_0, σ_0, n) = (0.001, 400 MPa, 0.15) are examined. The cohesive strength σ_c of both cases is set as 960 MPa, i.e. $\gamma = 2.4$. Under this condition, both cases are supposed to exhibit ductile fracture, in the absence of hydrogen. It is assumed that both 'materials' are susceptible to HE, and the HEDE mechanism dominates, i.e. σ_c is decreased by hydrogen following Eqs. (6) and (7), the influence of hydrogen on CGM is not addressed here. In addition, the hydrogen diffusion related parameters (Table 1) are supposed to be the same in both 'material' models, slow strain rate tension test is modelling to ensure that hydrogen has enough time to redistribute and reach equilibrium. The fracture behavior in the presence of hydrogen is simulated using the three-step hydrogen informed CZM scheme, elaborated in Section 2.2 and detailed in [52,53].

It is assumed that hydrogen is homogeneously distributed with an initial concentration C_i and different initial hydrogen concentrations are investigated. Under tensile loading, lattice hydrogen redistributes inside the specimen (Fig. 3) by stress driven diffusion. Trapped hydrogen concentration due to plastic strain is represented as a simplified function of the lattice concentration, following Olden et al [58,66]. The engineering stress-true strain (σ_e- ε) curves for M1 with $C_i = 1, 2, 3, 4$ wppm are shown in Fig. 13(a). The typical hydrogen promoted fracture is captured for $C_i = 2, 3, 4$ wppm and the fracture strain ε_f decreases as C_i increases. By applying a finer interval in C_i, the ε_f versus C_i curve is obtained, as shown in Fig. 13(b). The ε_f versus C_i curve has an inverted 'S' shape, this is consistent with experimental findings [17,61,75–77], where many mechanical characteristics including ductility versus hydrogen concentration shows a similar inverted 'S' shape. Results show that the hydrogen induced decrease in ε_f is gradual and that the ductile fracture is still observed when the amount of hydrogen is small, i.e. $C_i \leq 1.5$ wppm. This reveals the existence of a critical hydrogen concentration C_{Hc} above which the initiation of a transition phase appears, similarly to those observed in experiments [7,17,19–21]. When C_i is low, the material maintains sufficient cohesive strength and ductile fracture is still dominant, whereas when the concentration is high enough, a transition phase or a brittle lower shelf is observed.

The experimentally obtained inverted 'S' curve differs for different materials [61,75–77] and hence indicating varied critical hydrogen concentration C_{Hc}. It should be noted that the simulated inverted 'S' shaped curves are material dependent as well. Comparing M2 with M1, M2 features a shorter upper ductile shelf and considerably lower C_{Hc} than M1, implying that M2 is more sensitive to HE, although they display almost identical brittle shelf at high concentration. Usually, C_{Hc} is neglected and attention is paid mostly to the lower brittle shelf in the diagram, one of the reasons is that most HE susceptible materials are similar to M2 with very small C_{Hc} and a sharp transition phase. However, it is helpful to illustrate the existence of such an upper shelf, which shows that HE is phenomenologically comparable to low temperature embrittlement, thus bringing the different phenomena under a similar context. In addition, with the development in material design, it is highly possible that materials can possess an extended upper shelf, in which case the C_{Hc} and the transition phase need careful study.

Further, it is possible to estimate the critical hydrogen concentration C_{Hc} of a material using γ_c. γ_c is 'material' dependent. Given the basic plasticity parameters, which can be obtained by conventional mechanical tests, γ_c can be determined following the procedure described in Section 3. C_{Hc} can then be evaluated upon the calibration of the hydrogen degradation law. On the other hand, if the inverted 'S' diagram is experimentally obtained, the hydrogen degradation law can be deduced.

Finally, it should be noted that the conclusions, or rather the hypotheses, here are drawn from the parametric study using the perfect 'material' models. Although the inverted 'S' shaped curve has been revealed in many HE experiments, systematic testing of ductility loss versus hydrogen concentration curves in different materials is missing, the experimental validation needs to be done in the future. The challenge will be manufacturing a series of materials with different controlled properties.

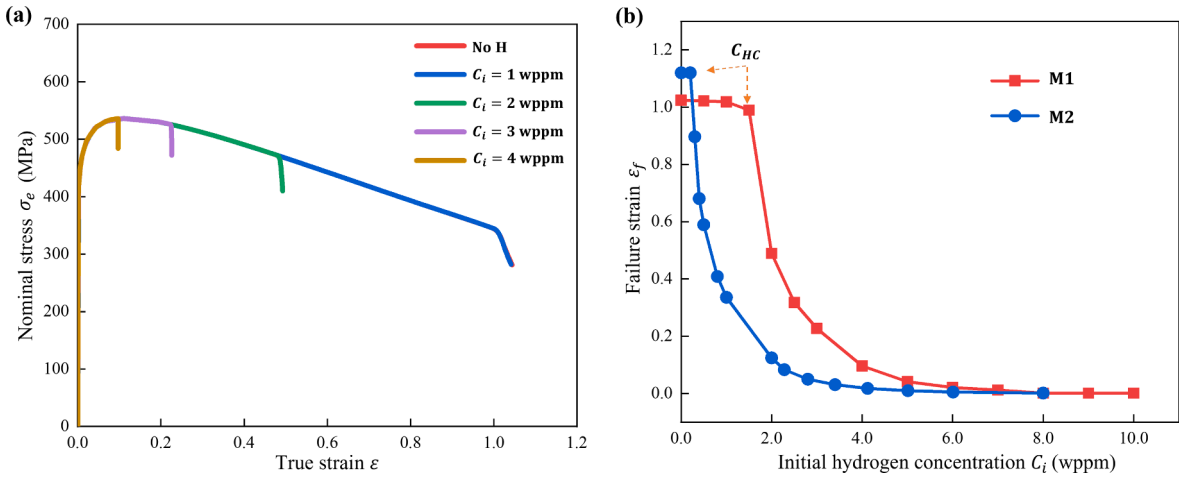

Fig. 13. (a) Engineering stress σ_e versus true strain ε curves for M1 with varying initial hydrogen concentration C_i; (b) Failure strain ε_f versus C_i for the representative 'materials', M1 and M2.

5. Summary

A general approach to simulating DBT in metallic material is established by combining CGM and CZM, and DBT is rationalized as the competition between ductile and brittle fracture. Materials with different mechanical properties, as well as various initial void volume fractions are investigated. The framework is applicable to BCC and some HCP metals in low temperature embrittlement scenario [78], as well as most BCC and some FCC metals [7,18–21,79] in HE scenario. In the present work, hydrogen induced DBT is simulated as a case study. The main conclusions are as follows.

(1) The proposed approach can capture both types of ductile and brittle fractures as well as their competition. The outcome of the competition depends on the strength ratio γ ($\gamma = \sigma_c/\sigma_0$) between cohesive strength σ_c and material's yield strength σ_0, brittle fracture occurs when the ratio is below a transition ratio γ_c. γ_c is material's parameter dependent and reflects the tendency towards brittle fracture.
(2) For a given material with initial voids, the failure strain ε_f versus γ diagram is 'S'-shaped, with an upper plateau and lower plateau and a transition phase. ε_f scales the material's resistance to fracture, while γ reveals the material's tendency to undergo brittle fracture. The transition ratio γ_c decreases with the increase of initial void volume fraction f_0 or yield strength σ_0, but increases with hardening exponent n. The influence of n is the most pronounced.
(3) For perfect model materials, γ is linked to hydrogen concentration C_H, and the failure strain ε_f versus concentration C_H diagram takes an inverted 'S'-shape. Corresponding to the transition ratio γ_c, there exists a critical hydrogen concentration C_{Hc} above which brittle fracture is triggered. It is noted that the complex interactions between hydrogen and microstructure in a real material may alter the shape of the curve, which needs to be further explored with experiments.

CRediT authorship contribution statement

Meichao Lin: Writing – review & editing, Writing – original draft, Visualization, Validation, Methodology, Investigation, Formal analysis, Conceptualization. **Haiyang Yu:** Investigation, Validation, Writing – review & editing, Formal analysis, Conceptualization. **Yu Ding:** Writing – review & editing, Investigation. **Vigdis Olden:** Validation, Writing – review & editing. **Antonio Alvaro:** Writing – review & editing, Validation. **Jianying He:** Validation, Writing – review & editing. **Zhiliang Zhang:** Writing – review & editing, Validation, Supervision, Funding acquisition.

Declaration of Competing Interest

The authors declare that they have no known competing financial interests or personal relationships that could have appeared to influence the work reported in this paper.

Acknowledgements

The authors appreciate the support provided by the Research Council of Norway through the HyLINE (294739) and M-HEAT (294689) projects.

Appendix A

The influence of critical separation δ_c on the transition ratio γ_c is explored, as shown in Fig. A.14. It shows that δ_c has limited effect on γ_c, since the initiation of brittle fracture, which is concerned in this study, is strength controlled.

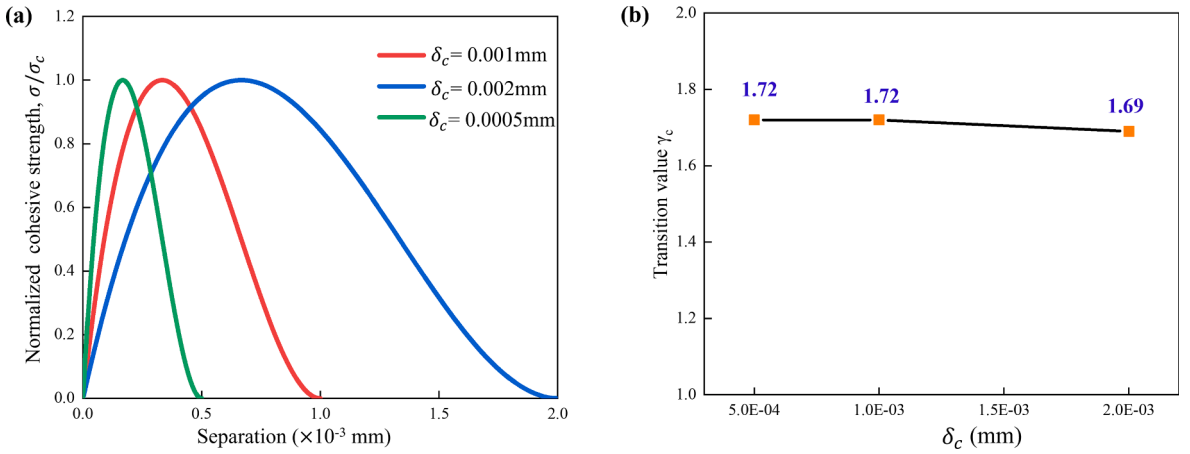

Fig. A.14. (a) Polynomial TSLs with different critical separation δ_c; (b) The transition ratio γ_c versus critical separation δ_c; the parameters $f_0 = 0.001$, $\sigma_0 = 400$ MPa, $n = 0.1$ are applied.

References

[1] Chao YJ, Ward JD, Sands RG. Charpy impact energy, fracture toughness and ductile–brittle transition temperature of dual-phase 590 Steel. Mater Des 2007;28(2):551–7.
[2] Hanamura T, Yin F, Nagai K. Ductile-brittle transition temperature of ultrafine ferrite/cementite microstructure in a low carbon steel controlled by effective grain size. ISIJ Int 2004;44(3):610–7.
[3] Ha KF, Yang C, Bao JS. Effect of dislocation density on the ductile-brittle transition in bulk Fe - 3%Si single crystals. Scr Metall Mater 1994;30(8):1065–70.
[4] Kim J-S, Kim Y-J, Lee M-W, Kim K-S, Shibanuma K. Fracture simulation model for API X80 Charpy test in Ductile-Brittle transition temperatures. Int J Mech Sci 2020;182:105771.
[5] Das S, Yu H, Tarleton E, Hofmann F. Hardening and Strain Localisation in Helium-Ion-Implanted Tungsten. Sci Rep 2019;9(1).
[6] McMahon CJ. Hydrogen-induced intergranular fracture of steels. Eng Fract Mech 2001;68(6):773–88.
[7] Wang D, Lu Xu, Wan Di, Guo X, Johnsen R. Effect of hydrogen on the embrittlement susceptibility of Fe–22Mn-0.6C TWIP steel revealed by in-situ tensile tests. Mater Sci Eng A 2021;802:140638.
[8] Cho L, Bradley PE, Lauria DS, Martin ML, Connolly MJ, Benzing JT, et al. Characteristics and mechanisms of hydrogen-induced quasi-cleavage fracture of lath martensitic steel. Acta Mater 2021;206:116635.
[9] Mao X, Qiao L. Hydrogen-induced cleavage fracture of Fe3Al-based intermetallics. Metall Mater Trans A 1996;27(12):3949–56.
[10] Laureys A, Depover T, Petrov R, Verbeken K. Influence of sample geometry and microstructure on the hydrogen induced cracking characteristics under uniaxial load. Mater Sci Eng A 2017;690:88–95.
[11] Wen J-F, Liu Y, Srivastava A, Benzerga AA, Tu S-T, Needleman A. Environmentally enhanced creep crack growth by grain boundary cavitation under cyclic loading. Acta Mater 2018;153:136–46.
[12] Huang J. Microstructural effect on the ductile-to-brittle transition in body centered cubic metals investigation by three dimensional dislocation dynamics simulations. Thesis for doctor of philosophy in mechanical and aerospace engineering. 2004.
[13] Harvey DP, Terrell JB, Sudarshan TS. Hydrogen effects on the ductile to brittle transition behaviour of 21-6-9 stainless steel. J Mater Sci 1994;29(20):5485–90.
[14] Sudarshan TS, Harvey DP, Place TA. Mechanistic similarities between hydrogen and temperature effects on the ductile-to-brittle transition of a stainless steel. Metall Trans A 1988;19(6):1547–53.
[15] Martínez-Pañeda E, Harris ZD, Fuentes-Alonso S, Scully JR, Burns JT. On the suitability of slow strain rate tensile testing for assessing hydrogen embrittlement susceptibility. Corros Sci 2020;163:108291.
[16] Pan C, Chu WY, Li ZB, Liang DT, Su YJ, Gao KW, et al. Hydrogen embrittlement induced by atomic hydrogen and hydrogen-induced martensites in type 304L stainless steel. Mater Sci Eng A 2003;351(1-2):293–8.
[17] Liu Y, Wang M, Liu G. Effect of hydrogen on ductility of high strength 3Ni–Cr–Mo–V steels. Mater Sci Eng A 2014;594:40–7.
[18] Djukic MB, Bakic GM, Sijacki Zeravcic V, Sedmak A, Rajicic B. The synergistic action and interplay of hydrogen embrittlement mechanisms in steels and iron: Localized plasticity and decohesion. Eng Fract Mech 2019;216:106528.
[19] Wang M, Akiyama E, Tsuzaki K. Determination of the critical hydrogen concentration for delayed fracture of high strength steel by constant load test and numerical calculation. Corros Sci 2006;48(8):2189–202.
[20] Kan B, Wu W, Yang Z, Li J. Stress-induced hydrogen redistribution and corresponding fracture behavior of Q960E steel at different hydrogen content. Mater Sci Eng A. 2020;775:138963.
[21] Trautmann A, Mori G, Oberndorfer M, Bauer S, Holzer C, Dittmann C. Hydrogen Uptake and Embrittlement of Carbon Steels in Various Environments. Materials (Basel) 2020;13(16):3604.
[22] Takakuwa O, Yamabe J, Matsunaga H, Furuya Y, Matsuoka S. Comprehensive Understanding of Ductility Loss Mechanisms in Various Steels with External and Internal Hydrogen. Metall Mater Trans A 2017;48(11):5717–32.
[23] Ding Y, Yu H, Zhao K, Lin M, Xiao S, Ortiz M, et al. Hydrogen-induced transgranular to intergranular fracture transition in bi-crystalline nickel. Scripta Mater 2021;204:114122.
[24] Oriani RA. A mechanistic theory of hydrogen embrittlement of steels. Ber Bunsenges Phys Chem 1972;76:848–57.
[25] Birnbaum HK, Sofronis P. Hydrogen-enhanced localized plasticity—a mechanism for hydrogen-related fracture. Mater Sci Eng A 1994;176(1-2):191–202.
[26] Benzerga AA, Leblond J-B. Ductile fracture by void growth to coalescence. Adv Appl Mech 2010;44:169–305.
[27] Le Roy G, Embury JD, Edwards G, Ashby MF. A model of ductile fracture based on the nucleation and growth of voids. Acta Metall 1981;29(8):1509–22.

[28] Luo T, Gao X. On the prediction of ductile fracture by void coalescence and strain localization. J Mech Phys Solids 2018;113:82–104.
[29] Gurson AL. Plastic flow and fracture behavior of ductile materials incorporating void nucleation, growth, and interaction. Brown University; 1975.
[30] Tvergaard V, Needleman A. Analysis of the cup-cone fracture in a round tensile bar. Acta Metall 1984;32(1):157–69.
[31] Ritchie RO, Knott JF, Rice JR. On the relationship between critical tensile stress and fracture toughness in mild steel. J Mech Phys Solids 1973;21(6):395–410.
[32] Beremin FM, Pineau A, Mudry F, Devaux J-C, D'Escatha Y, Ledermann P. A local criterion for cleavage fracture of a nuclear pressure vessel steel. Metall Trans A 1983;14(11):2277–87.
[33] Pineau A. Development of the local approach to fracture over the past 25 years: theory and applications. Int J Fract 2006;138:139–66.
[34] Klein PA, Foulk JW, Chen EP, Wimmer SA, Gao HJ. Physics-based modeling of brittle fracture: cohesive formulations and the application of meshfree methods. Theor Appl Fract Mech 2001;37(1-3):99–166.
[35] Hütter G, Linse T, Roth S, Mühlich U, Kuna M. A modeling approach for the complete ductile–brittle transition region: cohesive zone in combination with a non-local Gurson-model. Int J Fract 2014;185(1-2):129–53.
[36] Machado GA, Bittencourt E, Moresco RL. A Gurson model in association with a cohesive zone model on the investigation of cleavage-ductile transition in metals. Latin Am J Solids Struct 2021;18.
[37] Zhang ZL, Thaulow C, Ødegård J. A complete Gurson model approach for ductile fracture. Eng Fract Mech 2000;67(2):155–68.
[38] Thomason PF. Three-dimensional models for the plastic limit-loads at incipient failure of the intervoid matrix in ductile porous solids. Acta Metall 1985;33(6):1079–85.
[39] Needleman A. A Continuum Model for Void Nucleation by Inclusion Debonding. J Appl Mech 1987;54:525–31.
[40] Jemblie L, Olden V, Akselsen OM. A coupled diffusion and cohesive zone modelling approach for numerically assessing hydrogen embrittlement of steel structures. Int J Hydrogen Energy 2017;42(16):11980–95.
[41] Gobbi G, Colombo C, Miccoli S, Vergani L. A fully coupled implementation of hydrogen embrittlement in FE analysis. Adv Eng Softw 2019;135:102673.
[42] del Busto S, Betegón C, Martínez-Pañeda E. A cohesive zone framework for environmentally assisted fatigue. Eng Fract Mech 2017;185:210–26.
[43] Anderson TL. Fracture mechanics: fundamentals and applications. CRC Press; 2017.
[44] Gurson AL. Plastic Flow and Fracture Behavior of Ductile Materials, Incorporating Void Nucleation, Growth, and Interaction. Brown University; 1975.
[45] Sun D-Z, Kienzler R, Voss B, Schmitt W. Application of micromechanical models to the prediction of ductile fracture. Fracture Mechanics: Twenty-Second Symposium, vol. II. ASTM International; 1992.
[46] Zhang ZL, Hauge M. On the Gurson Micro-Mechanical Parameters. In: Panontin TL, Sheppard SD, editors. West Conshohocken. PA: ASTM International; 1999. p. 364–83.
[47] Zhang ZL. Explicit consistent tangent moduli with a return mapping algorithm for pressure-dependent elastoplasticity models. Comput Methods Appl Mech Eng 1995;121(1-4):29–44.
[48] Brocks W, Arafah D, Madia M. Exploiting symmetries of fe models and application to cohesive elements. Milano/Kiel 2013.
[49] Yu H, Olsen JS, Olden V, Alvaro A, He J, Zhang Z. Viscous regularization for cohesive zone modeling under constant displacement: An application to hydrogen embrittlement simulation. Eng Fract Mech 2016;166:23–42.
[50] Scheider I. Cohesive model for crack propagation analyses of structures with elastic plastic material behavior Foundations and implementation; 2002.
[51] Jemblie L, Olden V, Akselsen OM. A review of cohesive zone modelling as an approach for numerically assessing hydrogen embrittlement of steel structures. Philos Trans Roy Soc A Math Phys Eng Sci 2017;375(2098):20160411.
[52] Yu H, Olsen JS, Alvaro A, Olden V, He J, Zhang Z. A uniform hydrogen degradation law for high strength steels. Eng Fract Mech 2016;157:56–71.
[53] Yu H, Olsen JS, Olden V, Alvaro A, He J, Zhang Z. Cohesive zone simulation of grain size and misorientation effects on hydrogen embrittlement in nickel. Eng Fail Anal 2017;81:79–93.
[54] Serebrinsky S, Carter E, Ortiz M. A quantum-mechanically informed continuum model of hydrogen embrittlement. J Mech Phys Solids 2004;52:2403–30.
[55] Jiang DE, Carter EA. First principles assessment of ideal fracture energies of materials with mobile impurities: implications for hydrogen embrittlement of metals. Acta Mater 2004;52(16):4801–7.
[56] Alvaro A, Olden V, Akselsen OM. 3D cohesive modelling of hydrogen embrittlement in the heat affected zone of an X70 pipeline steel – Part II. Int J Hydrogen Energy 2014;39(7):3528–41.
[57] Colombo C, Zafra García A, Belzunce J, Fernandez Pariente I. Sensitivity to hydrogen embrittlement of AISI 4140 steel: A numerical study on fracture toughness. Theoret Appl Fract Mech 2020;110:102810.
[58] Olden V, Thaulow C, Johnsen R, Østby E, Berstad T. Influence of hydrogen from cathodic protection on the fracture susceptibility of 25%Cr duplex stainless steel – Constant load SENT testing and FE-modelling using hydrogen influenced cohesive zone elements. Eng Fract Mech 2009;76(7):827–44.
[59] Olden V, Thaulow C, Johnsen R, Østby E. Cohesive zone modeling of hydrogen-induced stress cracking in 25% Cr duplex stainless steel. Scr Mater 2007;57(7):615–8.
[60] Lin M, Yu H, Wang Xu, Wang R, Ding Yu, Alvaro A, et al. A microstructure informed and mixed-mode cohesive zone approach to simulating hydrogen embrittlement. Int J Hydrogen Energy 2022.
[61] Wang M, Akiyama E, Tsuzaki K. Effect of hydrogen on the fracture behavior of high strength steel during slow strain rate test. Corros Sci 2007;49(11):4081–97.
[62] Kim J, Gao X, Srivatsan TS. Modeling of void growth in ductile solids: effects of stress triaxiality and initial porosity. Eng Fract Mech 2004;71(3):379–400.
[63] Hu Y-M, Chen M-Z, Xiao Y, Xiao J, Tan X, Tang Q, et al. Parameters determination of GTN model and damage analysis of aluminum alloy 6016 sheet metal. In: Int Conf Mater Sci Appl(ICMSA 2015); 2015.
[64] Li J, Qiu Y-Y, Wang H-D, Wang Z-x. Estimation of the Strength Coefficient and Strain Hardening Exponent from Monotonic Tensile Properties of Steels. Int J Steel Struct 2019;19(6):1951–68.
[65] Zhongping Z, Weihua Wu, Donglin C, Qiang S, Wenzhen Z. New Formula Relating the Yield Stress-Strain With the Strength Coefficient and the Strain-Hardening Exponent. J Mater Eng Perform 2004;13(4):509–12.
[66] Olden V, Saai A, Jemblie L, Johnsen R. FE simulation of hydrogen diffusion in duplex stainless steel. Int J Hydrogen Energy 2014;39(2):1156–63.
[67] Tao P, Gong J, Wang Y, Cen W, Zhao J. Modeling of hydrogen diffusion in duplex stainless steel based on microstructure using finite element method. Int J Pres Ves Pip 2020;180:104031.
[68] Gholipour H, Biglari FR, Nikbin K. Experimental and numerical investigation of ductile fracture using GTN damage model on in-situ tensile tests. Int J Mech Sci 2019;164:105170.
[69] Nguyen O. Coarse-graining and renormalization of atomistic binding relations and universal macroscopic cohesive behavior. J Mech Phys Solids 2002;50:1727–41.
[70] Zhang ZL, Hauge M, Ødegård J, Thaulow C. Determining material true stress–strain curve from tensile specimens with rectangular cross-section. Int J Solids Struct 1999;36(23):3497–516.
[71] Zhang ZL, Hauge M, Thaulow C, Ødegård J. A notched cross weld tensile testing method for determining true stress–strain curves for weldments. Eng Fract Mech 2002;69(3):353–66.
[72] Tu S, Ren X, Nyhus B, Akselsen OM, He J, Zhang Z. A special notched tensile specimen to determine the flow stress-strain curve of hardening materials without applying the Bridgman correction. Eng Fract Mech 2017;179:225–39.
[73] Date CJ. The Principle of Orthogonal Design. Database Design and Relational Theory. Apress; 2019. p. 319–45.

[74] Turon A, Dávila CG, Camanho PP, Costa J. An engineering solution for mesh size effects in the simulation of delamination using cohesive zone models. Eng Fract Mech 2007;74(10):1665–82.
[75] Lovicu G, Bottazzi M, D'Aiuto F, De Sanctis M, Dimatteo A, Santus C, et al. Hydrogen Embrittlement of Automotive Advanced High-Strength Steels. Metall Mater Trans A 2012;43(11):4075–87.
[76] Dmytrakh IM, Leshchak RL, Syrotyuk AM. Effect of hydrogen concentration on strain behaviour of pipeline steel. Int J Hydrogen Energy 2015;40(10):4011–8.
[77] Wang M, Akiyama E, Tsuzaki K. Effect of hydrogen and stress concentration on the notch tensile strength of AISI 4135 steel. Mater Sci Eng A 2005;398(1-2):37–46.
[78] Chernov VM, Kardashev BK, Moroz KA. Low-temperature embrittlement and fracture of metals with different crystal lattices – Dislocation mechanisms. Nucl Mater Energy 2016;9:496–501.
[79] Koyama M, Akiyama E, Sawaguchi T, Raabe D, Tsuzaki K. Hydrogen-induced cracking at grain and twin boundaries in an Fe–Mn–C austenitic steel. Scr Mater 2012;66(7):459–62.